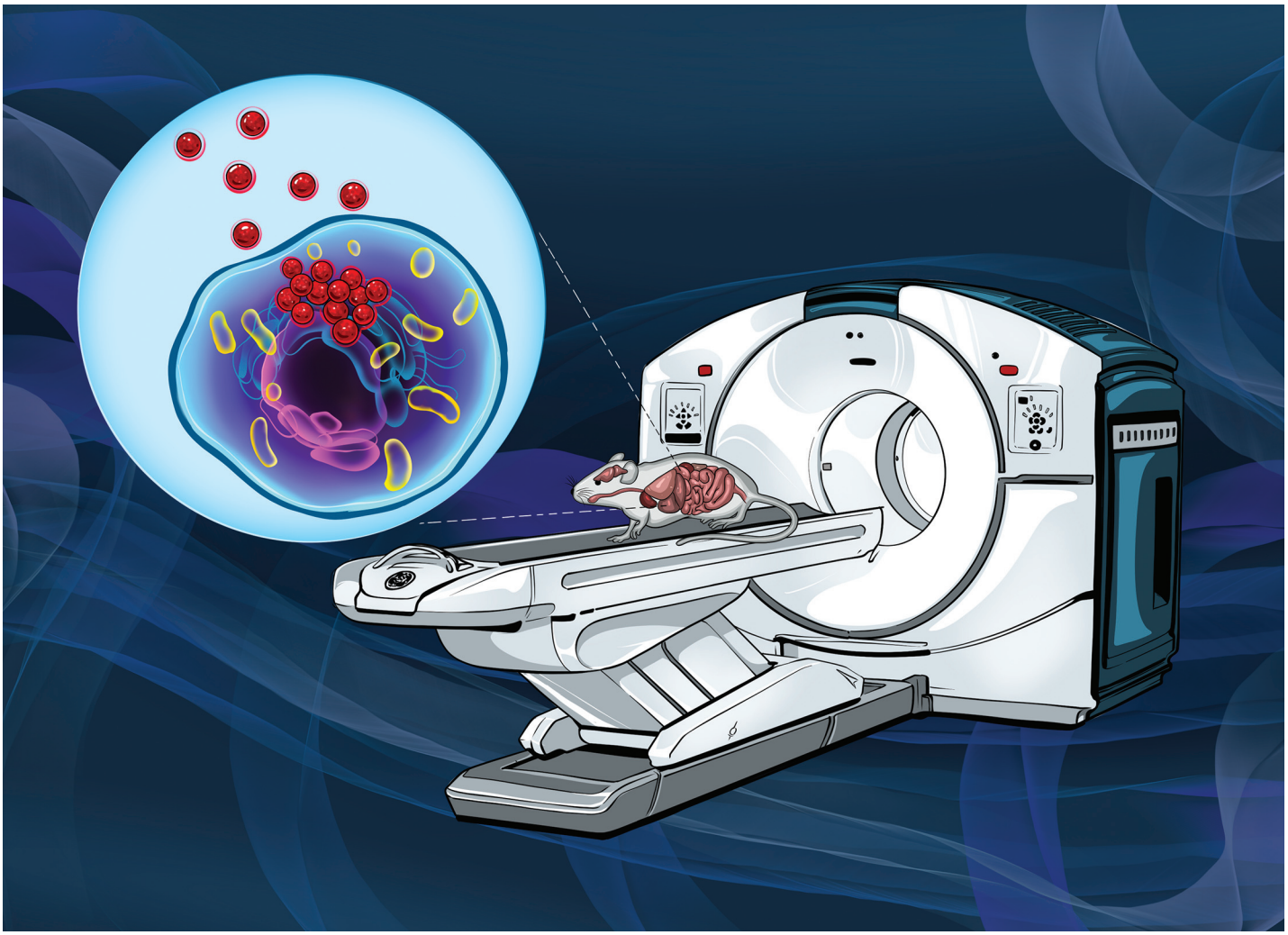

Novel research by Dr. Fabian Starsich and his colleagues from the Nanoparticle Systems Engineering Laboratory at ETH Zurich, Switzerland, and the University Medical Center Hamburg-Eppendorf, Germany.

Particle interactions and their effect on magnetic particle spectroscopy and imaging

Magnetic particle imaging (MPI) is an emerging medical diagnostic technique with immense potential for various clinical applications. Here, the rationalized design of high-performing multifunctional MPI nanotracers is described. Specifically, the importance of magnetic coupling phenomena following particle interactions and their effect on signal quality and stability is investigated.

As featured in:

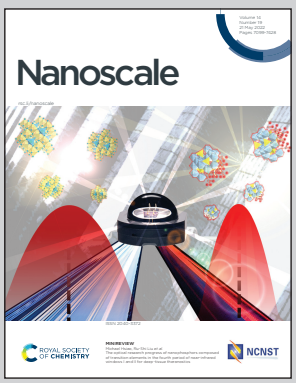

See Fabian H. L. Starsich *et al.*, *Nanoscale*, 2022, **14**, 7163.

ROYAL SOCIETY OF CHEMISTRY

rsc.li/nanoscale

Registered charity number: 207890

Nanoscale

ROYAL SOCIETY OF CHEMISTRY

PAPER

View Article Online
View Journal | View Issue

Cite this: *Nanoscale*, 2022, **14**, 7163

Particle interactions and their effect on magnetic particle spectroscopy and imaging†

Lorena Moor, [a] Subas Scheibler,[a,b] Lukas Gerken,[a,b] Konrad Scheffler, [c,d] Florian Thieben,[c,d] Tobias Knopp,[c,d] Inge K. Herrmann [a,b] and Fabian H. L. Starsich *[a,b]

Signal stability is crucial for an accurate diagnosis *via* magnetic particle imaging (MPI). However, MPI-tracer nanoparticles frequently agglomerate during their *in vivo* applications leading to particle interactions altering the signal. Here, we investigate the influence of such magnetic coupling phenomena on the MPI signal. We prepared $Zn_{0.4}Fe_{2.6}O_4$ nanoparticles by flame spray synthesis and controlled their inter-particle distance by varying SiO_2 coating thickness. The silica shell affected the magnetic properties indicating stronger particle interactions for a smaller inter-particle distance. The SiO_2-coated $Zn_{0.4}Fe_{2.6}O_4$ outperformed the bare sample in magnetic particle spectroscopy (MPS) in terms of signal/noise, however, the shell thickness itself only weakly influenced the MPS signal. To investigate the importance of magnetic coupling effects in more detail, we benchmarked the MPS signal of the bare and SiO_2-coated Zn-ferrites against commercially available PVP-coated Fe_3O_4 nanoparticles in water and PBS. PBS is known to destabilize nanoparticle colloids mimicking *in vivo*-like agglomeration. The bare and coated Zn-ferrites showed excellent signal stability, despite their agglomeration in PBS. We attribute this to their process-intrinsic aggregated morphology formed during their flame-synthesis, which generates an MPS signal only little affected by PBS. On the other hand, the MPS signal of commercial PVP-coated Fe_3O_4 strongly decreased in PBS compared to water, indicating strongly changed particle interactions. The relevance of this effect was further investigated in a human cell model. For PVP-coated Fe_3O_4, we detected a strong discrepancy between the particle concentration obtained from the MPS signal and the actual concentration determined *via* ICP-MS. The same trend was observed during their MPI analysis; while SiO_2-coated Zn-ferrites could be precisely located in water and PBS, PVP-coated Fe_3O_4 could not be detected in PBS at all. This drastically limits the sensitivity and also general applicability of these commercial tracers for MPI and illustrates the advantages of our flame-made Zn-ferrites concerning signal stability and ultimately diagnostic accuracy.

Received 22nd December 2021,
Accepted 19th March 2022

DOI: 10.1039/d1nr08402j

rsc.li/nanoscale

Introduction

Magnetic particle imaging (MPI) is an emerging diagnostic method with various promising application areas. It is based on the non-linear response of magnetic nanoparticles to an applied oscillating magnetic field.[1] The tracer particles are injected and accumulate *via* active or passive targeting mechanisms at the site of interest. A static magnetic field with strong gradients is applied to saturate the majority of the particles in the tissue and only create a small field-free region.[2] An oscillating magnetic field is superimposed to the static magnetic field and only the signal of the MPI tracers in the field-free region is detected *via* coils. The field-free region is then swept over the entire volume of interest (field of view) to obtain a three-dimensional image.[3] The main advantage of MPI lies in its high sensitivity down to 10^{-6}–10^{-8} M.[4] As only the tracers are imaged, there is no disturbance through background signals created by the tissue itself. MPI does not require harmful ionizing radiation, in contrast to frequently used positron emission tomography (PET). Furthermore, this comparably inexpensive imaging technique stands out due to its high spatial and temporal resolution outperforming clinically established methods such as magnetic resonance imaging (MRI) or computer tomography (CT).

[a]*Nanoparticle Systems Engineering Laboratory, Department of Mechanical and Process Engineering, ETH Zurich, Sonneggstrasse 3, 8092 Zurich, Switzerland. E-mail: fabiasta@ethz.ch; Tel: +41 44 632 84 92*
[b]*Particles-Biology Interactions, Department Materials Meet Life, Swiss Federal Laboratories for Materials Science and Technology (Empa), Lerchenfeldstrasse 5, 9014 St. Gallen, Switzerland*
[c]*Section for Biomedical Imaging, University Medical Center Hamburg-Eppendorf, Lottestraße 55, 22529 Hamburg, Germany*
[d]*Institute for Biomedical Imaging, Hamburg University of Technology, Am Schwarzenberg-Campus 3, 21073 Hamburg, Germany*
† Electronic supplementary information (ESI) available. See DOI: https://doi.org/10.1039/d1nr08402j

The overall MPI performance strongly depends on the exact tracer characteristics.[4] The magnetization of these nanoparticles is frequently described *via* the Langevin function.[2] However, the latter neglects the relaxation mechanisms (*i.e.* Néel- and Brownian relaxation) present in larger particles and caused by thermal perturbations. These result in a delay of the magnetic response to the field, which drastically complicates the tracer dynamics. Surprisingly, research on the practical optimization of these nanoparticles is still in its infancy. Previous studies have frequently used commercially available materials or clinically approved MRI contrast agents based on iron oxides. While this approach would potentially allow a swift translation of the tracers into clinics provided that human-sized MPI scanners become feasible, the investigated systems are far from ideal for this application. In fact, according to simulations, only 3% of the iron mass of the clinically approved Ferucarbotran (Resovist) dispersion contributes to the MPI signal. The major part was suggested to remain inactive due to its too small size.[1] Follow-up studies indicated that this mass might increase by a factor of 30 due to particle interactions.[5] While ferucarbotran based nanoparticles are still used as the standard MPI tracers, attempts to improve signal strength through material engineering have been reported. So far, they have focused on size-optimizations of polymer-coated iron oxide nanoparticles.[6] However, a deeper understanding of the involved mechanisms especially under physiologically relevant conditions is yet to be achieved.

Next to signal intensity, also, signal stability is crucial for a reliable and accurate diagnosis *via* nanoparticle-based imaging methods. In this regard, particle interactions play a fundamental role.[7] Nanoparticles are frequently characterized as monodisperse non-interacting spheres in aqueous dispersions *ex vivo*. Upon their injection *in vivo* or their exposure to cells *in vitro*,[8,9] they agglomerate due to the harsher conditions faced.[10] These changes in the surroundings include variations in the salt concentration, pH, or protein adsorption as well as internalization into subcellular compartments. As a result of the agglomeration, the primary particles are in close contact leading to particle–particle interactions. Magnetic nanoparticles will couple, which strongly alters their overall magnetic properties.[11] This phenomenon has been investigated for various sensing applications *via* MRI[12,13] or MPS.[14] Interestingly, however, it has been frequently neglected otherwise. Polymer coatings only slightly improve the stability and in long run have been shown to even disintegrate exposing the bare particle surface.[15] We have recently succeeded in reducing the coupling of ultrasmall iron oxide nanoparticles by the introduction of a silica support material.[16] The addition of silica during flame spray pyrolysis kept the effective magnetic size of the iron oxide clusters below the paramagnetic limit yielding a strong MRI T1 contrast.

Analogous investigations for MPI tracers, however, are scarce. Recently, such magnetic interactions have been termed superferromagnetism and investigated for signal enhancements.[17] Moreover, Khandhar *et al.* showed that the signal of commercial polymer-coated nanoparticles decreases by 53% in the cell-culture medium compared to water.[18] They attributed this reduction to particle interactions and resulting changes in magnetic relaxation.[19] The obtained signal could no longer be assigned to a specific particle concentration *via* a calibration curve, as the latter strongly depends on the exact particle state, which is typically unknown. These particle interactions were also investigated by encapsulating commercial polymer-coated iron oxide particles into red blood cells.[20] The obtained MPS signals of the cells with the tracers revealed a strong discrepancy to the reference samples in water. Such differences between effective and predicted tracer concentrations are highly problematic.[21] It drastically increases the risks of false diagnoses caused by over- or underpredictions of tracer quantities. Simulation work investigating the MPI response of monodisperse particles[22] and particle chains[23] also shows the importance of magnetic interactions.

In this work, we aim to investigate and mitigate this risk by controlling particle interactions through core–shell structures. To this end, we utilize versatile flame-synthesis, which has been previously investigated for the synthesis of a wide range of magnetic nanomaterials of different sizes,[24] compositions,[25] and morphologies.[26] More specifically, we investigate SiO_2-coated non-stoichiometric Zn-ferrites with improved magnetic properties compared to pure iron oxides and high biocompatibility.[27] We focus on analyzing and optimizing MPS signal stability under physiologically relevant conditions.

Experimental methods

Particle synthesis

$Zn_{0.4}Fe_{2.6}O_4$ nanoparticles were produced by flame spray pyrolysis, as previously described.[26,27] A liquid precursor solution was fed at 5 mL min^{-1} through a capillary and dispersed by 5 L min^{-1} O_2 into fine droplets. These are ignited by flaming CH_4/O_2 mixture (1.5 and 3.2 L min^{-1}, respectively), which then leads to the primary particle formation. The flame is further surrounded by 40 L min^{-1} of O_2 sheath gas. The particle stream is guided *via* a quartz glass tube (length 20 cm, inner diameter 45 mm) through the SiO_2 coating ring. The latter has 16 openings facing 30° downwards the particle stream and is positioned right on top of the tube leading to an injection height above the burner of 20 cm. HMDSO (hexamethyldisiloxane, Sigma-Aldrich) vapor is injected through the openings, which condenses on the freshly formed core particles and forms the SiO_2 layer. The HMDSO vapor is fed *via* an N_2 stream saturated in a bubbler and further diluted by 16 L min^{-1} N_2. The SiO_2 content in the final product is controlled through the N_2 bubbler flow and calculated at saturation conditions (T = 20 °C, $p_{vapor,HMDSO}$ = 43 mbar, wt% SiO_2 = $m_{SiO_2}/(m_{SiO_2} + m_{Zn_{0.4}Fe_{2.6}O_4})$. The stream of the now SiO_2 coated $Zn_{0.4}Fe_{2.6}O_4$ particles is guided *via* another quartz glass tube (length 30 cm, inner diameter 45 mm) onto a glass fiber filter (Whatman GF6, 257 mm diameter), where the particles are collected with the help of a vacuum pump (Busch, Seco SV 1040C).

Before the synthesis, the precursor solution for the $Zn_{0.4}Fe_{2.6}O_4$ nanoparticles was prepared at a concentration of 0.2 mol_{Zn+Fe} L^{-1} in a 3 : 1 volume ratio of xylene and acetonitrile (both Sigma-Aldrich). Iron acetylacetonate (Sigma-Aldrich) and zinc acetylacetonate (Sigma-Aldrich) were dissolved accordingly *via* magnetic stirring for 1 h at room temperature. HMDSO was utilized in the bubbler as supplied.

PVP (polyvinylpyrrolidone) – coated Fe_3O_4 was purchased from Nanocomposix (NanoXact Magnetite Nanoparticles – PVP – 20 mg mL^{-1} in aqueous 2 mM sodium citrate, 20 nm ± 5 nm).

Characterization

X-ray diffraction patterns were recorded on a Bruker D2 Phaser (30 kV, mA). The obtained data was analyzed *via* Diffrac Eva and TOPAS 4.2. software. XRD intensity spectra were fitted over all angles (2θ) to the standard pattern of magnetite (Fe_3O_4, IDSC: 84611) and crystal size computed *via* Rietveld refinement.

Scanning transmission electron microscopy (STEM) was performed on a Talos F200x microscope (ThermoFisher, field emission gun at 200 kV) with four attached silicon drift detectors. Samples were prepared by dispersing nanoparticles in mili-Q ultra-pure water. A dispersion drop was deposited on a carbon-coated copper grid (EMR, Lacey Carbon Film 200 Mesh Copper) and then carefully dried. The primary core particle size distribution was estimated by measuring the longest axis of 176 bare and 103 70 wt% SiO_2 coated $Zn_{0.4}Fe_{2.6}O_4$ nanoparticles using ImageJ software and convergence of geometrical standard deviation was ensured. Log–normal size distribution was assumed.

Dynamic light scattering analysis for hydrodynamic size and ζ-potential was conducted on a Zetasizer (Nano ZS90 Malvern Instruments). Samples were prepared by dispersing the nanoparticles in mili-Q ultra-pure water or PBS (phosphate buffered saline) at a concentration of 0.1 mg mL^{-1} *via* 10 minutes of sonication (Ultrasonic Processor, pulses: 28 s/2 s, 90% Amplitude).

Magnetic properties were assessed *via* VSM on a Quantum Design Physical Property Measurement System. The samples were prepared by measuring the weight of the particles and placing them between two capillaries. The magnetization *versus* applied field curves (*MH*-curves) was assessed at 300 K. The applied field ranged from 3000 mT to −3000 mT. Zero-field cooled (ZFC) and field cooled (FC) curves were obtained by varying the temperature in the range from 10 K to 300 K and applying a magnetic field of 150 Oe for FC.

Magnetic particle spectroscopy and imaging

To investigate the particle response under a sinusoidal magnetic field, a custom-made and calibrated magnetic particle spectrometer (MPS) similar to a previous study[28] was used. An MPS is essentially an MPI-scanner without spatial encoding. A time-dependent magnetization curve is measured *via* coils by exciting the particles in one dimension. The base frequency of the magnetic field was set to 26.042 kHz and the amplitude to 20 mT. For further understanding of particle behavior, the spectrum of the magnetization curve is investigated in the frequency domain. The harmonics of the base frequency can be used to compare the response of different particles and their general suitability for MPI.

In addition to the particle characterization *via* onedimensional MPS excitation, the particles were investigated regarding their applicability for imaging using a preclinical MPI-scanner (Bruker, Germany). To this end, two-dimensional system matrices were measured using a point source which is driven through the field of view by a robot. A system matrix describes the system's response of every discrete voxel for every frequency component and is needed to reconstruct the particle signal from the received voltage signal. The system matrices for 8 μL cubic particle samples (17 g L^{-1} in water) were measured using a gradient of 2 T m^{-1} and a drive field strength of 12 mT leading to a field of view of 24 × 24 mm discretized in 13 × 13 voxels of size 1.85 × 1.85 mm. A signal-to-noise threshold of 5 was applied together with a minimum frequency of 80 kHz. For a good spatial resolution of the reconstructed image, particles should give clear system matrix patterns for as many frequency components as possible. The investigation of the decay of the system matrix's amplitude over the harmonics is therefore a crucial measure to compare different particles in their suitability for MPI imaging. Images were reconstructed with the open-access Julia package MPIReco[29] using an iterative regularized Kaczmarz algorithm, a relaxation parameter λ of 0.001, and 100 iterations.

For the *in vitro* experiments, human soft tissue sarcoma cells (HT1080, ATCC) were seeded at 250 000 per T25 flask in 7.2 mL medium and left to attach for 24 h. 800 μL of 1 mg mL^{-1} nanoparticle dispersion in ultra-pure water (after ultrasonication) were added for a final concentration of 0.1 mg mL^{-1}. After 24 h of incubation cells were washed twice with PBS (phosphate buffered saline) and then trypsinized using 500 μL Trypsin. Trypsinization was quenched with 1 mL MEM (minimum essential medium). Thereafter, the supernatants were removed and replaced by 500 μL 4%PFA (paraformaldehyde) in PBS. After 4 h, PFA was replaced with 1.5 mL PBS. The cells were spun down and transferred in 100 μL to fresh Eppendorf tubes. Next, the cells were centrifuged and the cell pellet was resuspended in 20 μL of 0.5% agar (diluted from hot 1.5% agar using prewarmed PBS) and the samples were put in a freezer for 10 min. Finally, 100 μL Mowiol was added on top for protection and left to harden overnight at room temperature.

For ICP-OES samples, all washings, as well as the cell pellets, were collected separately to distinguish intra- and extracellular particles and digested at 250 °C in concentrated nitric acid and hydrogen peroxide using a microwave (turboWAVE Inert, MLS GmbH, Leutkirch, Germany). Samples were diluted using ultra-pure water to reach a final concentration of 2% nitric acid. Fe and Zn contents were determined by an ICP-OES 5110 (Agilent, Basel, Switzerland) instrument with external calibration ranging from 0 to 5 ppm.

Results and discussion

To investigate the importance of particle interactions on MPI, bare and SiO_2 coated $Zn_{0.4}Fe_{2.6}O_4$ nanoparticles were prepared by scalable flame synthesis. The SiO_2 shell is applied *in situ*,[30] which allows the coating of individual core particles and thus gives control over their interparticle (core-to-core) distance. Fig. 1 (top) shows scanning electron microscopy images of the prepared bare (a) and 70 wt% SiO_2-coated (b) $Zn_{0.4}Fe_{2.6}O_4$ nanoparticles. The homogenous SiO_2 shell surrounding the predominantly hexagonal particles is visible. This leads to a clear separation of the magnetic $Zn_{0.4}Fe_{2.6}O_4$ core in comparison to the bare sample. Both images show that the primary particles for bare and the SiO_2 shell matrix for coated samples are connected *via* sinter necks to larger aggregates, which is characteristic of flame-made nanomaterials.[31]

The as-prepared nanoparticles were further analyzed concerning their morphology and composition. The table in Fig. 1 (bottom) summarizes the results. The XRD patterns (see Fig. S1†) of the bare and all SiO_2-coated particles are indicative of the desired spinel ferrite structure.[32] The crystal size lies between 14 and 15 nm is unaffected by the SiO_2 coating. This is in agreement with previous reports on *in situ* SiO_2 coated flame-made nanoparticles[33] and shows that the coating was applied after the core particle formation had been completed. The particle composition was verified through ICP-MS revealing an actual stoichiometry of $Zn_{0.35}Zn_{2.65}O_4$ and $Zn_{0.36}Zn_{2.64}O_4$ for the bare and 70 wt% SiO_2-coated particles, respectively. The geometrical mean core diameters determined from TEM analysis ($d_{TEM,core}$) are in agreement with the crystal sizes and show a geometric standard deviation σ_g of 1.4. The agglomerate size measured in water (d_{DLS}) slightly increases for increasing SiO_2 contents, as expected for a thicker shell. The complete coating even for the lowest SiO_2 content is suggested by the shown constant ζ-potentials for all coated samples. The ζ-potential values show a distinct decrease from +14 mV for bare $Zn_{0.4}Fe_{2.6}O_4$ to −28 mV for all SiO_2-coated particles, in agreement with the literature.[27]

Next, the prepared nanomaterials were analyzed in detail concerning their magnetic properties. Fig. 2a shows the magnetization curves normalized to the total sample mass (incl. SiO_2). All samples show an S-shaped data set characteristic to ferro- and ferrimagnetic systems. There is no major hysteresis detectable, indicating that the magnetic sizes of the particles are within the superparamagnetic range (*i.e.* <appr. 25 nm for Fe_3O_4 [34]). As summarized in Table 1, the coercivity H_c decreases from 0.86 mT for the bare to 0.39 mT for the 70 wt% SiO_2-coated sample. This trend corresponds to previously

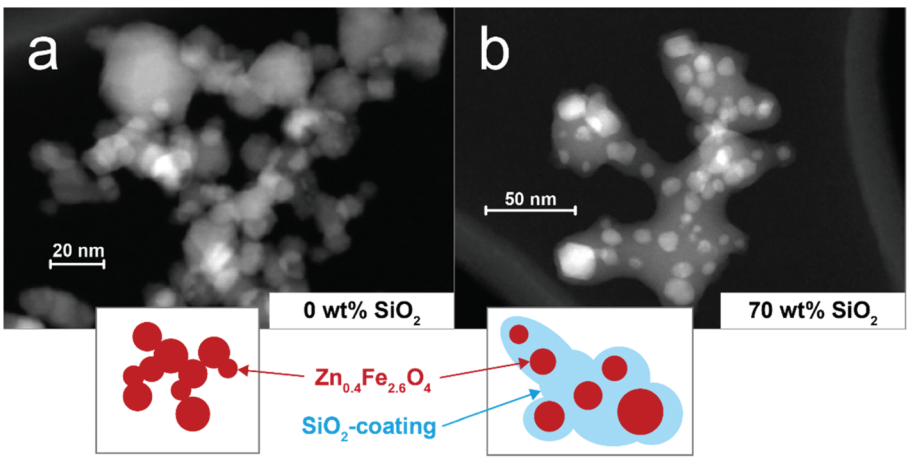

	d_{XRD} [nm]	$d_{TEM,core}$ [nm]	σ_g	d_{DLS} [nm]	ζ-pot [mV]
$Zn_{0.4}Fe_{2.6}O_4$ - 0 wt% SiO_2	14.2	14.5	1.4	107.2	14.3 ± 4.5
$Zn_{0.4}Fe_{2.6}O_4$ - 15 wt% SiO_2	14.8			115.5	-27.1 ± 3
$Zn_{0.4}Fe_{2.6}O_4$ - 50 wt% SiO_2	14.6			125.3	-28.8 ± 5.2
$Zn_{0.4}Fe_{2.6}O_4$ - 70 wt% SiO_2	14.3	11.6	1.4	145.4	-28.2 ± 3.9

Fig. 1 STEM images of as-prepared (a) bare and (b) 70 wt% SiO_2-coated $Zn_{0.4}Fe_{2.6}O_4$ nanoparticles. Insets schematically depict characteristic morphology. Table (below) summarizes morphological characteristics of the different prepared particles: crystal sizes (d_{XRD}), geometric mean primary particle sizes of core ($d_{TEM,core}$), geometrical standard deviations of primary particle sizes of core (σ_g), geometric means of hydrodynamic diameter (d_{DLS}), ζ-potentials (ζ-pot).

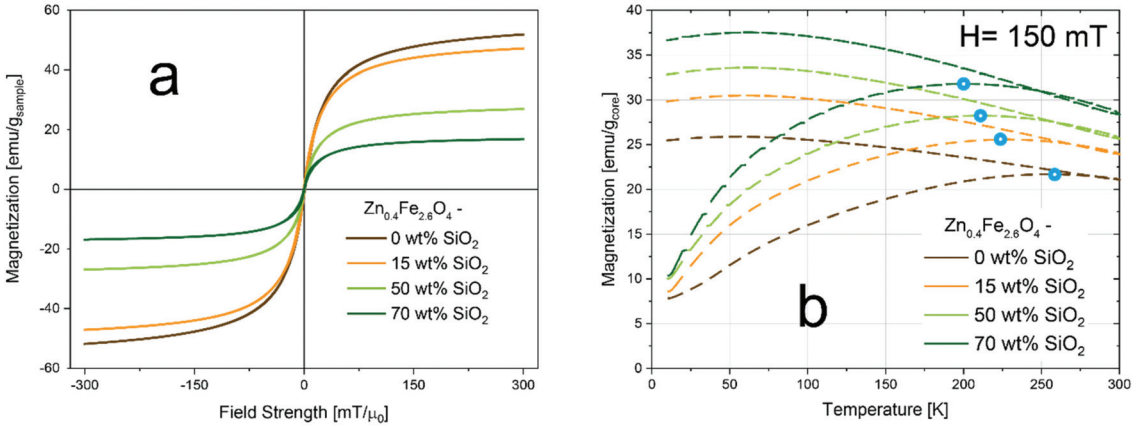

Fig. 2 (a) Magnetizations per mass of overall sample as function of applied field. (b) Magnetizations per mass of overall sample as a function of temperature at a constant applied field of 150 mT (*i.e.* field-cooling curves). Blocking temperatures are indicated by a blue hollow sphere.

Table 1 Summary of magnetic properties extracted from magnetization and field-cooling curves: saturation magnetizations (M_s) per mass of overall samples and per nominal mass of magnetic core, coercivities (H_c), magnetic susceptibilities (χ), blocking temperatures (T_B)

	M_s		H_c	χ	T_B
	[emu g_{sample}^{-1}]	[emu g_{core}^{-1}]	[mT]	[1/mT]	[K]
$Zn_{0.4}Fe_{2.6}O_4$ – 0 wt% SiO_2	59	59	0.86	0.03	252
$Zn_{0.4}Fe_{2.6}O_4$ – 15 wt% SiO_2	52.7	62	0.72	0.036	227
$Zn_{0.4}Fe_{2.6}O_4$ – 50 wt% SiO_2	29.7	59.4	0.31	0.047	215
$Zn_{0.4}Fe_{2.6}O_4$ – 70 wt% SiO_2	18.1	60.3	0.39	0.059	201

reported data on flame-made γ-Fe_2O_3 of similar size,[35] while for larger $Zn_{0.4}Fe_{2.6}O_4$ nanoparticles (d_{XRD} = 29 nm) an increase in coercivity with the SiO_2-coating has been observed.[27] This highlights the importance but also complexity of magnetic interactions. While the values for the saturation magnetization M_s per sample mass decrease for increasing SiO_2 contents as expected, they remain constant at approximately 60 emu g^{-1} if normalized to the nominal core mass. This value[27] and trend[35] correspond to the literature and suggest that the volume and the composition of the magnetic core are not affected by the SiO_2 coating, which is in agreement with the constant d_{XRD}.

The susceptibility χ increases for thicker SiO_2 shells. This trend is also evident in Fig. 2b, which shows the field-cooled curves *i.e.* the magnetization normalized by the nominal core mass at an applied field of 150 mT as a function of temperature for all samples. The magnetization at 300 K increases similarly to χ, indicating a more pronounced magnetic response for the coated samples at low applied fields compared to the bare particles. The blocking temperatures (T_B, blue marks) refer to the transition from the magnetically blocked to the superparamagnetic state. At this temperature, the magnetic dipole moments possess enough thermal energy to overcome the applied field and can thus rotate freely. The T_B values shift towards lower temperatures for higher SiO_2 contents. This indicates reduced magnetic dipole interactions due to increased inter-particle distances caused by the coating.[36] Overall, through the incorporation of Zn into the iron oxide matrix we could decrease the coercivity and increase the saturation magnetization of the material in comparison to previously reported flame-made pure iron oxide particles.

The above-discussed influence of particle interactions on magnetic properties has been measured under quasi-static applied fields *via* vibrating sample magnetometry (VSM). However, in MPI oscillating magnetic fields at drastically higher frequencies are employed, which strongly affects the magnetic response due to the involved dipole relaxation mechanisms.

To this end, the prepared particles were analyzed concerning the imaging performance *via* magnetic particle spectroscopy (MPS, *i.e.* MPI without spatial encoding). MPS detects the response of magnetic nanoparticles to an oscillating magnetic field *via* voltage induction in a coil. Fig. 3 summarizes the performance of the prepared bare and SiO_2-coated $Zn_{0.4}Fe_{2.6}O_4$ in the time and frequency domain. All measurements were performed using aqueous dispersions at a constant nominal magnetic core concentration to directly compare the magnetic properties. Fig. 3a shows the obtained voltage signal over time and Fig. 3b the absolute signal as a function of the applied field. The signal amplitude increases clearly with increasing SiO_2 shell thickness, despite the constant amount of magnetic mass. Although measured at different frequencies this is in excellent agreement with the susceptibility trend shown above (Table 1). The magnetic spec-

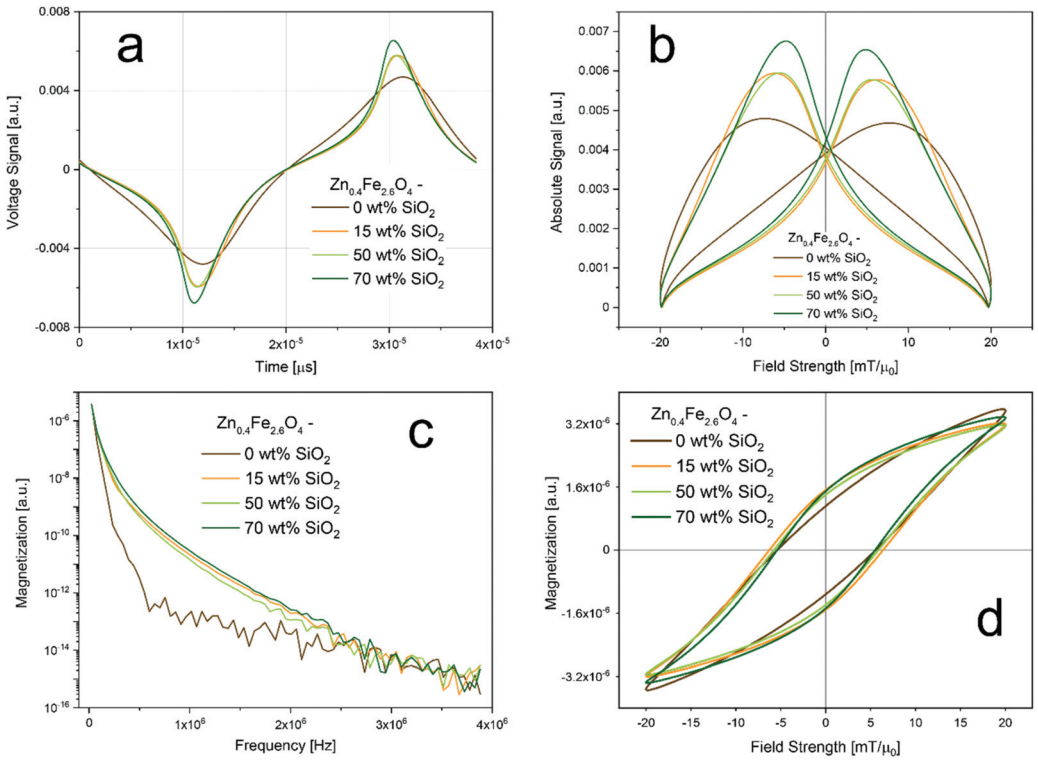

Fig. 3 MPS results: (a) measured signal as function of time; (b) measured signal as a function of applied field (*i.e.* point spread function); (c) magnetization as a function of frequency (*i.e.* magnetic spectrum); (d) magnetization as a function of applied field strength (*i.e.* hysteresis). Measurements were conducted at 20 mT with a frequency of 26 kHz and at a constant nominal magnetic material concentration of 17 g L^{-1}.

trum shown in Fig. 3c (*i.e.* Fourier-transform of Fig. 3a) confirms the observations by showing clear differences between the bare and all SiO_2-coated samples over all frequencies. However, the influence of the coating thickness is only minor. Fig. 3d depicts the hysteresis curves derived from the MPS signals. The maximal magnetizations remain almost constant for all samples. Differences are mostly detectable in the slopes as also shown in Fig. 3b. Interestingly, coercivity values remain almost constant for all samples. This is not in agreement with the VSM data shown above (Table 1), where a small decrease with increasing silica shell thickness was observed. However, it emphasizes the strong dependence of the magnetic properties on the frequency of the applied changing field.

To investigate this behavior and the effect of magnetic interactions in more detail, we conducted MPS measurements in different dispersion media. The obtained amplitudes of the signal harmonics (*i.e.* multiples of magnetic field frequency) show good linear agreement with the particle concentration down to 16 μg mL^{-1}. Even though frequently used in literature, the voltage amplitude is sufficiently linear only down to approximately 1 mg mL^{-1} (see Fig. S2†). Fig. 4a depicts the 3rd harmonic MPS signals as a function of particle concentration in water and PBS (phosphate buffered saline). Data is shown for bare and SiO_2-coated (70 wt%) $Zn_{0.4}Fe_{2.6}O_4$, as well as commercial PVP (polyvinylpyrrolidone) – coated Fe_3O_4. The latter belongs to the group of commonly used MPI tracers in literature (*i.e.* polymer-coated iron oxides).[4] Although PVP-coated Fe_3O_4 has the strongest signal in water, it also loses most of its performance in PBS. Our flame-made bare and SiO_2-coated Zn-ferrites, on the other hand, show comparably constant calibration lines. In the 15th harmonic (Fig. 4b), the SiO_2-coated Zn-ferrite particles distinctively outperform the other systems while still attaining good stability over the dispersion medium. This trend is further analyzed in Fig. 4c, which depicts the slopes of the calibration lines as a function of the signal harmonics for all samples in water and PBS. PVP-coated Fe_3O_4 nanoparticles show steeper slopes at lower harmonics than the flame-made particles. For the 7th and higher harmonics, however, SiO_2-coated $Zn_{0.4}Fe_{2.6}O_4$ nanoparticles show the best performance. The signal of commercial polymer-coated particles continuously decreases reaching a signal value of 10^{-12} at the 13th harmonic which is typically used as the detection limit. At this point, SiO_2-coated Zn-ferrite nanoparticles outperform PVP-coated Fe_3O_4 by more than two orders of magnitude. The signal stability over the dispersion medium is further analyzed in Fig. 4d, which shows the ratio of the calibration line slopes in PBS over water. Our flame-made bare and SiO_2-coated Zn-ferrites show excellent signal stability throughout all harmonics. Interestingly, the bare particles attain a slightly steeper calibration curve in PBS compared to H_2O. Potentially, this can be explained by superferromagnetic behavior, as recently described.[17] Particles in an agglomerate/aggregate experience, next to the applied external magnetic field, also the magnetic field originating from their already

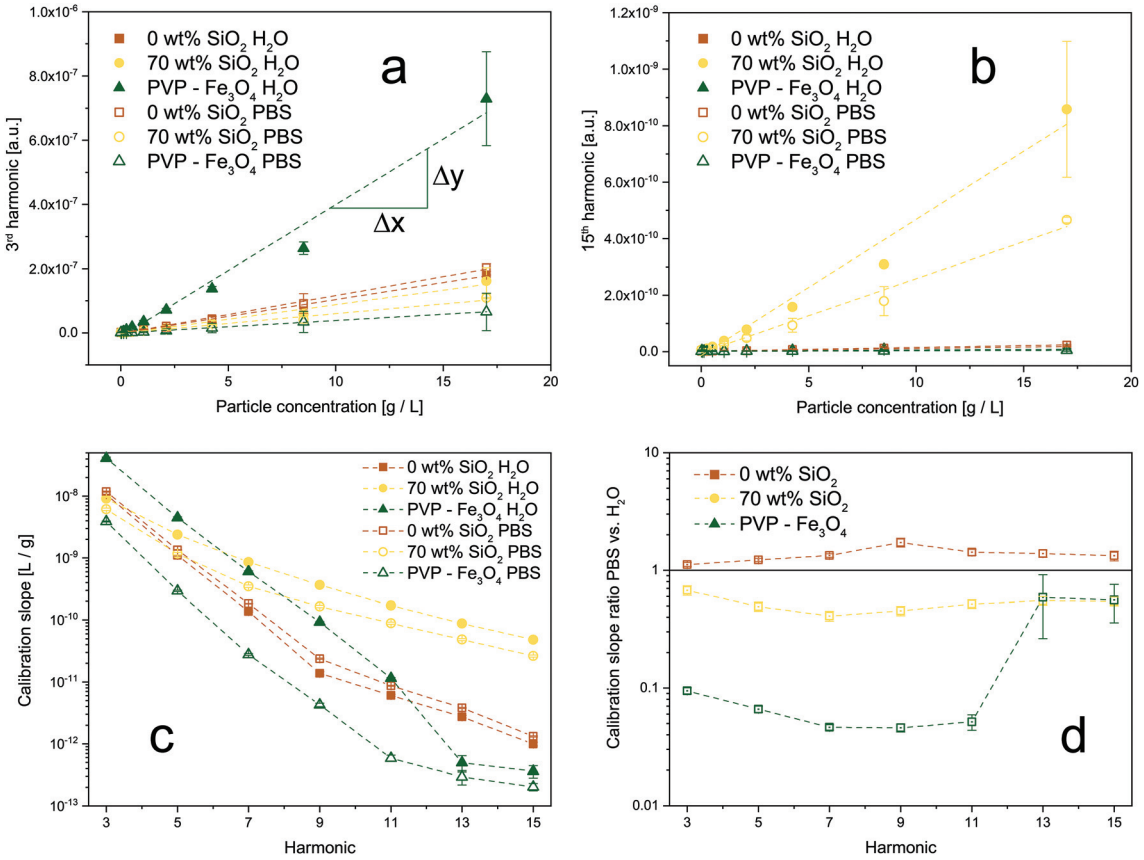

Fig. 4 Comparison of signal stability as a function of dispersion medium for synthesized Zn-ferrites and commercial magnetite nanoparticles. Calibration curves for (a) 3rd and (b) 15th harmonic for bare and SiO_2-coated (70 wt%) $Zn_{0.4}Fe_{2.6}O_4$, as well as commercial PVP (polyvinylpyrrolidone)-coated Fe_3O_4, dispersed in H_2O (closed symbols) or PBS (open symbols). (c) The slope of the calibration lines as a function of the harmonics for all samples in H_2O and PBS. (d) The ratio of the calibration slopes in PBS over H_2O for all particles. A value close to 1 indicates a stable signal. Samples were measured at the same overall particle concentrations (core + shell).

magnetized neighboring particles. This results in an "avalanche" magnetization if the particles are in close proximity, as given here for the bare system. The strong agglomeration of the particles in PBS might enhance this effect, leading to a stronger magnetic response and thus steeper calibration curves compared to H_2O. On the other hand, PVP-coated Fe_3O_4 suffers from a big discrepancy between the signals measured in H_2O and PBS. The sudden increase at the 13th harmonic most likely is an artifact from the weak signal ($<10^{-12}$) at these frequencies, which is also reflected in the larger error bars.

The aforementioned results can be explained by changes in their state of agglomeration. Khandhar *et al.* reported a similar trend with MPS signal voltage decreases of 8%, 53%, and 74% in blood, cell-culture medium, and 1 wt% agar gel, respectively.[18] Fig. S3† shows the hydrodynamic diameters of the samples measured in water and PBS. While the flame-made particles attain a size of approximately 100 nm in H_2O, the commercial PVP-coated Fe_3O_4 has a size of approximately 30 nm. Interestingly, upon exposure to PBS bare, 15 wt% and 50 wt% SiO_2-coated Zn-ferrites, as well as the commercial PVP-coated Fe_3O_4 show a strong size increase to 400 or even 1000 nm and above. This increase corresponds to literature and can be explained by the high ionic strength of PBS and the thus weakened repulsive forces leading to stronger agglomeration.[37] The hydrodynamic diameter of SiO_2-coated (70 wt%) $Zn_{0.4}Fe_{2.6}O_4$ nanoparticles, on the other hand, remains constant or even slightly decreases. We attribute this effect to the excessive SiO_2-content in the system, which enhances the dispersibility of the particles compared to the bare or thinner coated Zn-ferrites. Although the increased agglomeration is observed also for bare Zn-ferrites, instabilities in the MPS signal are only observable for PVP-coated Fe_3O_4. Firstly, we attribute this to a stronger size increase of the commercial particles in PBS compared to water. Secondly, this can be explained by morphological differences between materials. The prepared bare and SiO_2-coated Zn-ferrites show a strongly aggregated structure (Fig. 1) characteristic of flame-made nanoparticles.[31] This is a result of their high-temperature synthesis leading to the formation of strong sinter-necks between the primary particles, which remain stable even during harsh dispersion conditions. As a result, the magnetic cores have a fixed distance (bare: touching, SiO_2-coated: separated) and thus magnetic coupling originating from their synthesis. Additional agglomeration in dispersion does not substantially

affect these interactions. PVP-coated Fe_3O_4, on the other hand, is characterized as monodisperse non-interacting particles in water. Upon their exposure to PBS, they strongly agglomerate leading to particle interactions despite the polymer coating. Ultimately, this results in a highly unstable MPS signal. This experiment simplistically mimics the conditions faced by nanoparticles *in vitro* and *in vivo*, causing unavoidable agglomeration.[7] This is especially problematic as the obtained MPI signals are typically assigned to particle concentrations *via* external calibration curves.

To analyze the limitations of quantitative MPS/MPI under more realistic conditions, bare and SiO_2-coated Zn-ferrites, as well as commercial PVP-coated Fe_3O_4 nanoparticles were incubated with cells for 24 h. The precise amount of particles taken up by the cells was determined *via* ICP-MS. The cell samples were then analyzed *via* MPS. Signal harmonics or particle concentrations predicted through the calibration lines were then compared to the effective values determined by ICP-OES. Fig. 5a shows the ratio of the MPS signal harmonics determined through the calibrations using the exact particle concentration over the actual MPS signal. Throughout all relevant harmonics, SiO_2-coated Zn-ferrites show the best accuracy, with comparable signal ratios for H_2O and PBS dispersions. The good performance of PVP-coated Fe_3O_4 at higher harmonics can be explained again by low signal intensities. A similar trend can be observed in Fig. 5b, which shows the error of the particle concentrations determined *via* the MPS signal. SiO_2-coated Zn-ferrites show a comparably good prediction of the particle concentration throughout all signal harmonics. PVP-coated Fe_3O_4, on the other hand, drastically underpredicts the concentration by at least 65%. At higher harmonics, these particles perform especially poorly with errors above 100% (data not shown).

However, the underprediction of the concentrations can be observed for all samples and both water and PBS calibrations curves. This can be explained by the fixation of the cells and thus also the particles in a polymer, which suppresses Brownian relaxation mechanisms and in the following the overall MPS signal. For SiO_2-coated Zn-ferrite, the PBS calibrations result in better accuracy. Most likely, this is a result of the increased particle agglomeration in PBS better mimicking the *in vitro* morphology. Nevertheless, it has to be mentioned that even for the best performing SiO_2-coated Zn-ferrites in PBS the average error in concentration over all harmonics lies at around 33%. This value increases to 57% when using the calibration in water. This highlights the importance of magnetic particle interaction and shows the current limitations of quantitative MPS and MPI.

In a final step, we investigate the consequences of the particle and thus signal stability on the actual magnetic particle imaging performance. To this end, we obtained the system matrix at 13^2 different locations in a 2D MPI setup for SiO_2-coated (70 wt%) $Zn_{0.4}Fe_{2.6}O_4$, as well as commercial PVP-coated Fe_3O_4 dispersed in H_2O or PBS at the same overall particle concentration. Bare Zn-ferrites could not be analyzed due to too strong sedimentation of particles during the measurement time. Fig. 6a shows the obtained system matrices for the 66^{th} frequency component (k) for all samples. Distinct patterns can be observed for the SiO_2-coated Zn-ferrites indicating a good signal-to-noise ratio both in water and PBS. In contrast, the polymer-coated particles show the characteristic system matrix features only in aqueous dispersion, while no signal could be detected in PBS. These observations are confirmed by data in Fig. 6b, which show the MPI signal as a function of the harmonics for all samples. PVP-coated Fe_3O_4 in H_2O results in a high signal at low harmonics, which quickly declines thereafter. Flame-made SiO_2-coated Zn-ferrites show excellent signal strength in both media, especially at higher harmonics, where they outperform the commercial polymer-coated particles. Differences between the signals in PBS *versus* water are depicted in Fig. 6d. SiO_2-Coated (70 wt%) $Zn_{0.4}Fe_{2.6}O_4$ particles show excellent signal stability over the entire harmonic range.

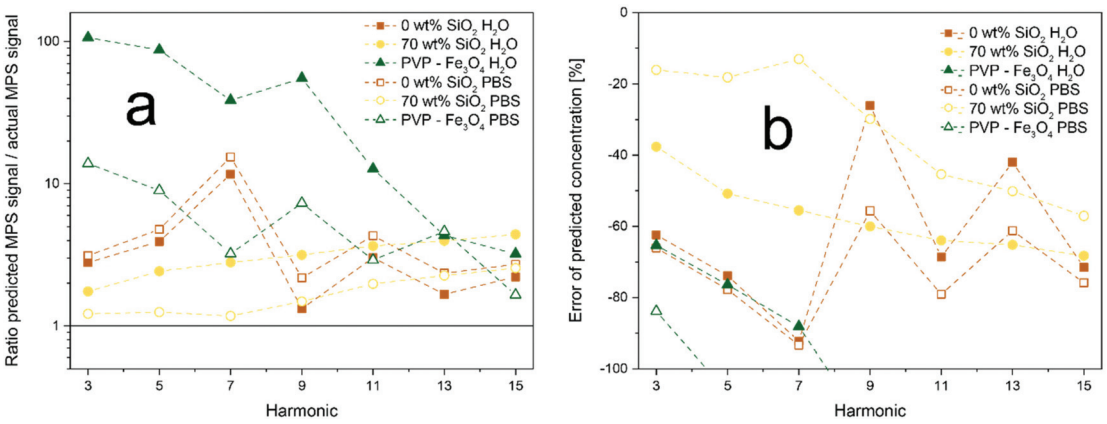

Fig. 5 Signal stability *in vitro*. Particles were incubated with cells for 24 h and their concentration and MPS signal after washing were determined. Data is shown for bare and SiO_2-coated (70 wt%) $Zn_{0.4}Fe_{2.6}O_4$, as well as commercial PVP-coated Fe_3O_4 dispersed in H_2O (closed symbols) or PBS (open symbols). (a) Ratio of MPS signals predicted at the measured particle concentration through calibration curves and actual measured MPS signal. (b) Error of particle concentration determined *via* MPS calibration curves.

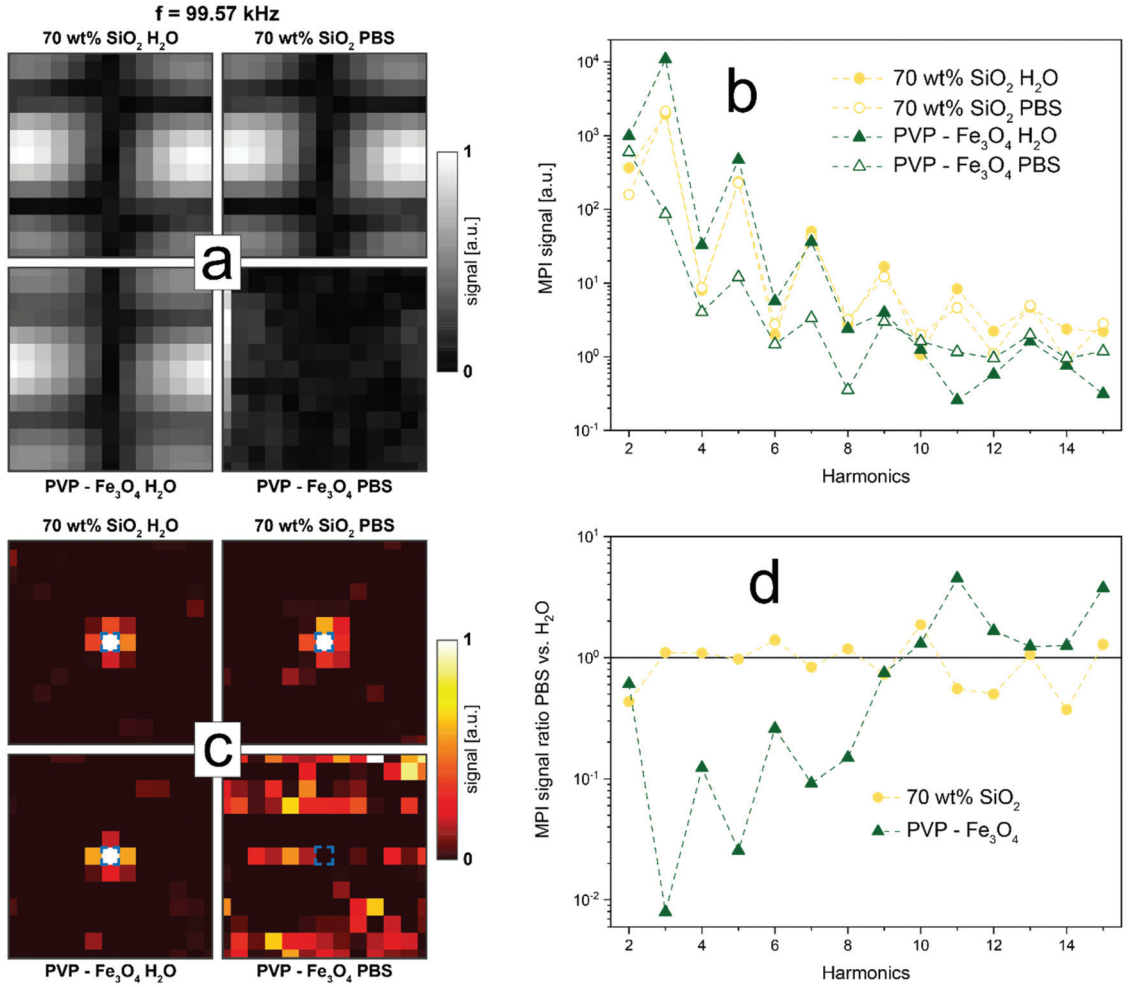

Fig. 6 Influence of dispersion medium on MPI quality of SiO_2-coated (70 wt%) $Zn_{0.4}Fe_{2.6}O_4$, as well as commercial PVP-coated Fe_3O_4, dispersed in H_2O or PBS at 17 g L^{-1}. (a) Absolute values of the system matrices at 99.57 kHz. Values are normalized to sample maximum. (b) Signal at the particle location as a function of the signal harmonics. (c) Reconstructed images of all samples. Signals are normalized to sample maximum. Blue square indicates particle location. (d) Ratio of signal measured in H_2O over PBS at the particle location as a function of the signal harmonics.

They distinctively outperform PVP-coated Fe_3O_4, which shows signal differences of up to two orders of magnitude. This discrepancy is further reflected in the reconstructed images depicted in Fig. 6c, using the respective system matrices in H_2O or PBS. As expected, SiO_2-coated Zn-ferrites can be precisely located in water and PBS, while only aqueous PVP-coated Fe_3O_4 results in a satisfactory image. The same holds if the system matrices obtained in H_2O are used for the reconstruction of the PBS samples (data not shown).

Conclusions

Nanoparticle agglomerations as well as the resulting particle interactions *in vitro* and *in vivo* are frequently neglected. However, their consequences ranging from changes in bio-distribution or altered magnetic characteristics, as described here, are severe. Here, we report that magnetic particle imaging is strongly affected by such magnetic coupling effects.

We found a distinctly better MPS signal for SiO_2-coated compared to bare Zn-ferrites. However, the exact thickness of the shell did not substantially influence the signal. The dependence of the exact MPS-signal spectrum on the particle characteristics will be a topic of future research. Most importantly, both here prepared systems showed a constant MPS signal, irrespective of their dispersion medium. Conversely, frequently used polymer-coated Fe_3O_4 nanoparticles drastically lost signal intensity at the same particle concentration in PBS compared to water. We explain the stability of our here prepared Zn-ferrite tracers by their pre-aggregated state yielding an MPS signal only little affected by nanoparticle agglomeration in physiological fluids.

Signal stability is crucial for the exact quantification of tracer amounts during the magnetic particle imaging process. This quantifiability is a frequently mentioned key advantage of MPI compared to other imaging methods, which, however, might be limited when using gold-standard polymer-coated nanoparticles. We illustrated this issue by comparing actual

particle concentrations (measured by ICP-MS) to values obtained from MPS *via* calibration curves in water. We detected a clear discrepancy for commercial PVP-coated Fe_3O_4, while especially SiO_2-coated Zn-ferrites showed good agreement between measured and effective concentration.

The manifestation of this effect was also observable in magnetic particle imaging. SiO_2-coated (70 wt%) $Zn_{0.4}Fe_{2.6}O_4$ tracers could be clearly located in water and PBS, while PVP-coated Fe_3O_4 lost most of its signal in PBS rendering them unsuitable for MPI.

Our study highlights the critical importance of signal stability and how it might be affected by conditions faced by magnetic particle tracers upon *in vitro* and *in vivo* application. Our pre-aggregated Zn-ferrite tracers offer a promising route to overcome the challenges of signal instability induced by particle agglomeration effects. The investigation of their *in vivo* performance, as well as potential MPI signal evaluation, approaches to further reduce the effect of particle agglomeration on signal stability are topics for necessary research in the near future.

Conflicts of interest

There are no conflicts to declare.

Acknowledgements

We acknowledge Raphael Langenegger for his contributions and thank Alexander Gogos for the microscopy images. The table of contents entry was partly created with BioRender.com. We thank the Swiss National Science Foundation for generous funding through the Eccellenza (181290) and the Scientific Exchange scheme (IZSEZ0_205894). This work was supported by an ETH Career Seed Grant funded through the ETH Zurich Foundation.

References

1 B. Gleich and J. Weizenecker, *Nature*, 2005, **435**, 1214–1217.
2 T. Knopp and T. M. Buzug, *Magnetic Particle Imaging*, Springer Berlin Heidelberg, Berlin, Heidelberg, 2012.
3 J. Weizenecker, B. Gleich, J. Rahmer, H. Dahnke and J. Borgert, *Phys. Med. Biol.*, 2009, **54**, L1–L10.
4 L. M. Bauer, S. F. Situ, M. A. Griswold and A. C. S. Samia, *J. Phys. Chem. Lett.*, 2015, **6**, 2509–2517.
5 D. Eberbeck, F. Wiekhorst, S. Wagner and L. Trahms, *Appl. Phys. Lett.*, 2011, **98**, 182502.
6 N. Panagiotopoulos, R. L. Duschka, M. Ahlborg, G. Bringout, C. Debbeler, M. Graeser, C. Kaethner, K. Lüdtke-Buzug, H. Medimagh, J. Stelzner, T. M. Buzug, J. Barkhausen, F. M. Vogt and J. Haegele, *Int. J. Nanomed.*, 2015, **10**, 3097–3114.
7 F. H. L. Starsich, I. K. Herrmann and S. E. Pratsinis, *Annu. Rev. Chem. Biomol. Eng.*, 2019, **10**, 155–174.
8 A. Spyrogianni, G. A. Sotiriou, D. Brambilla, J.-C. Leroux and S. E. Pratsinis, *J. Aerosol Sci.*, 2017, **108**, 56–66.
9 A. Spyrogianni, K. S. Karadima, E. Goudeli, V. G. Mavrantzas and S. E. Pratsinis, *J. Chem. Phys.*, 2018, **148**, 064703.
10 T. L. Moore, L. Rodriguez-Lorenzo, V. Hirsch, S. Balog, D. Urban, C. Jud, B. Rothen-Rutishauser, M. Lattuada and A. Petri-Fink, *Chem. Soc. Rev.*, 2015, **44**, 6287–6305.
11 S. Mørup, M. F. Hansen and C. Frandsen, *Beilstein J. Nanotechnol.*, 2010, **1**, 182–190.
12 L. Josephson, J. M. Perez and R. Weissleder, *Angew. Chem.*, 2001, **113**, 3304–3306.
13 J. M. Perez, L. Josephson, T. O'Loughlin, D. Högemann and R. Weissleder, *Nat. Biotechnol.*, 2002, **20**, 816–820.
14 S. Müssig, B. Kuttich, F. Fidler, D. Haddad, S. Wintzheimer, T. Kraus and K. Mandel, *Nanoscale Adv.*, 2021, **3**, 2822–2829.
15 N. C. Ataman and H.-A. Klok, *Macromolecules*, 2016, **49**, 9035–9047.
16 F. H. L. Starsich, C. Eberhardt, K. Keevend, A. Boss, A. M. Hirt, I. K. Herrmann and S. E. Pratsinis, *ACS Appl. Bio Mater.*, 2018, **1**, 783–791.
17 Z. W. Tay, S. Savliwala, D. W. Hensley, K. L. B. Fung, C. Colson, B. D. Fellows, X. Zhou, Q. Huynh, Y. Lu, B. Zheng, P. Chandrasekharan, S. M. Rivera-Jimenez, C. M. Rinaldi-Ramos and S. M. Conolly, *Small Methods*, 2021, **5**, 2100796.
18 A. P. Khandhar, R. M. Ferguson, H. Arami and K. M. Krishnan, *Biomaterials*, 2013, **34**, 3837–3845.
19 M. Möddel, C. Meins, J. Dieckhoff and T. Knopp, *New J. Phys.*, 2018, **20**, 083001.
20 A. Antonelli, P. Szwargulski, E.-S. Scarpa, F. Thieben, G. Cordula, G. Ambrosi, L. Guidi, P. Ludewig, T. Knopp and M. Magnani, *Nanomedicine*, 2020, **15**, 739–753.
21 E. Teeman, C. Shasha, J. E. Evans and K. M. Krishnan, *Nanoscale*, 2019, **11**, 7771–7780.
22 K. Them, *Phys. Med. Biol.*, 2017, **62**, 5623–5639.
23 Z. Zhao and C. Rinaldi, *Phys. Med. Biol.*, 2020, **65**, 185013.
24 R. Strobel and S. E. Pratsinis, *Adv. Powder Technol.*, 2009, **20**, 190–194.
25 I. K. Herrmann, R. N. Grass, D. Mazunin and W. J. Stark, *Chem. Mater.*, 2009, **21**, 3275–3281.
26 F. H. L. Starsich, C. Eberhardt, A. Boss, A. M. Hirt and S. E. Pratsinis, *Adv. Healthcare Mater.*, 2018, **7**, 1800287.
27 F. H. L. Starsich, G. A. Sotiriou, M. C. Wurnig, C. Eberhardt, A. M. Hirt, A. Boss and S. E. Pratsinis, *Adv. Healthcare Mater.*, 2016, **5**, 2698–2706.
28 S. Biederer, T. Knopp, T. F. Sattel, K. Lüdtke-Buzug, B. Gleich, J. Weizenecker, J. Borgert and T. M. Buzug, *J. Phys. D: Appl. Phys.*, 2009, **42**, 205007.
29 T. Knopp, P. Szwargulski, F. Griese, M. Grosser, M. Boberg and M. Möddel, *Int. J. Mag. Part. Imag.*, 2019, **5**, 907001.
30 A. Teleki, M. C. Heine, F. Krumeich, M. K. Akhtar and S. E. Pratsinis, *Langmuir*, 2008, **24**, 12553–12558.
31 M. L. Eggersdorfer and S. E. Pratsinis, *Adv. Powder Technol.*, 2014, **25**, 71–90.

32 Y. Yang, X. Liu, Y. Yang, W. Xiao, Z. Li, D. Xue, F. Li and J. Ding, *J. Mater. Chem. C*, 2013, **1**, 2875–2885.
33 A. Teleki, M. Suter, P. R. Kidambi, O. Ergeneman, F. Krumeich, B. J. Nelson and S. E. Pratsinis, *Chem. Mater.*, 2009, **21**, 2094–2100.
34 A. G. Kolhatkar, A. C. Jamison, D. Litvinov, R. C. Willson and T. R. Lee, *Int. J. Mol. Sci.*, 2013, **14**, 15977–16009.
35 A. M. Hirt, G. A. Sotiriou, P. R. Kidambi and A. Teleki, *J. Appl. Phys.*, 2014, **115**, 044314.
36 E. S. D. T. de Mendonça, A. C. B. de Faria, S. C. L. Dias, F. F. H. Aragón, J. C. Mantilla, J. A. H. Coaquira and J. A. Dias, *Surf. Interfaces*, 2019, **14**, 34–43.
37 J. Lim, S. P. Yeap, H. X. Che and S. C. Low, *Nanoscale Res. Lett.*, 2013, **8**, 381.